A&A 677, A7 (2023)
https://doi.org/10.1051/0004-6361/202346626

Astronomy & Astrophysics

Modeling of the nebular-phase spectral evolution of stripped-envelope supernovae

New grids from 100 to 450 days

L. Dessart[1], D. John Hillier[2], S. E. Woosley[3], and H. Kuncarayakti[4,5]

[1] Institut d'Astrophysique de Paris, CNRS-Sorbonne Université, 98 bis boulevard Arago, 75014 Paris, France
e-mail: dessart@iap.fr
[2] Department of Physics and Astronomy & Pittsburgh Particle Physics, Astrophysics, and Cosmology Center (PITT PACC), University of Pittsburgh, 3941 O'Hara Street, Pittsburgh, PA 15260, USA
[3] Department of Astronomy and Astrophysics, University of California, Santa Cruz, CA 95064, USA
[4] Tuorla Observatory, Department of Physics and Astronomy, 20014 University of Turku, Finland
[5] Finnish Centre for Astronomy with ESO (FINCA), 20014 University of Turku, Finland

Received 9 April 2023 / Accepted 21 June 2023

ABSTRACT

We present an extended grid of multi-epoch 1D nonlocal thermodynamic equilibrium radiative transfer calculations for nebular-phase Type Ibc supernovae (SNe) from He-star explosions. Compared to our previous work, which was focused on a post-explosion epoch of 200 days, here we study the spectral evolution from 100 to about 450 days. We also augment the model set with progenitors that evolved without wind mass loss. Models with the same final, pre-SN mass have similar yields and produce essentially the same emergent spectra. Hence, the uncertain progenitor mass loss history compromises the inference of the initial, main sequence mass. This shortcoming does not affect Type IIb SNe in which mass-loss has left a small residual H-rich envelope in the progenitor star at core collapse and, hence, an intact He core. However, our 1D models with a different pre-SN mass tend to yield widely different spectra, as seen through variations in the strong emission lines due to [N II] $\lambda\lambda$ 6548, 6583, [O I] $\lambda\lambda$ 6300, 6364, [Ca II] $\lambda\lambda$ 7291, 7323, [Ni II] λ 7378, and the forest of Fe II lines below 5500 Å. At the lower mass end, the ejecta are He-rich, and at 100 days, they cool through He I, N II, Ca II, and Fe II lines, with N II and Fe II dominating at 450 days. These models, associated with He giants, stand in conflict to observed SNe Ib, which typically lack strong N II emission. Instead, they may lead to SNe Ibn or, because of additional stripping by a companion star, ultra-stripped SNe Ic. In contrast, for higher pre-SN masses, the ejecta are progressively He poor and cool at 100 days through O I, Ca II, and Fe II lines, with O I and Ca II dominating at 450 days. Non-uniform, aspherical, large-scale mixing is more likely to determine the SN type at intermediate pre-SN masses, rather than any compositional differences. Variations in clumping and mixing, as well as departures from spherical symmetry would increase the spectral diversity, but also introduce additional degeneracies. More robust predictions from spectral modeling thus require that careful attention be paid to the initial conditions by incorporating the salient features of physically consistent 3D explosion models.

Key words. radiative transfer – supernovae: general – line: formation

1. Introduction

In a previous work (Dessart et al. 2021a, hereafter D21), we performed non-local thermodynamic equilibrium (non-LTE) radiative transfer calculations with the code CMFGEN (Hillier & Dessart 2012), employing the He-star progenitor and explosion models of Woosley (2019) and Ertl et al. (2020). These explorations were focused on a SN age of 200 days and complemented earlier calculations for similar He-star models that focused on the photospheric phase (Dessart et al. 2020; Woosley et al. 2021). Here, we extend the study of D21 to cover the nebular phase from 100 to about 450 days after explosion for the He-star models of D21, with an initial mass between 2.6 and 12.0 $M_\odot$ (corresponding to masses between 13.85 and 35.74 $M_\odot$ on the H zero-age main sequence).

The aim of this work is to compute Type Ib and Ic SN observables associated with He star models covering from the lowest mass massive stars undergoing core collapse up to higher mass He stars just below the threshold for black hole formation and implosion (Ertl et al. 2020). Objects at the lower mass end are favored by the initial mass function but their complicated physics (nuclear flashes) and special properties (large radii) might lead to peculiar SNe rather than standard Type Ib SNe (see, e.g., the recent works of Yoon 2015; Kleiser et al. 2018; or Woosley 2019). At the high mass end, He stars die without a He-rich shell (He/N or He/C) and represent ideal candidates for Type Ic SNe (Dessart et al. 2020). Because of the fundamental asymmetric nature of the neutrino-driven explosion mechanism and the resulting 3D asymmetric, distribution of elements (Wongwathanarat et al. 2015; Gabler et al. 2021), non-thermal excitation of He may vary from SN to SN and with viewing angle. Thus objects with similar pre-SN mass of say 6 $M_\odot$ may appear as Type Ib or Type Ic (Dessart et al. 2012). In the present work, spherical symmetry is assumed so that the division between Type Ib and Type Ic is sharp (probably too much so) and is tied to the presence or absence of the He/N shell in the progenitor at the moment of explosion (Dessart et al. 2020).

Only a small number of works have been devoted to the numerical modeling of stripped-envelope SNe at nebular epochs. Non-LTE models have been produced for Type IIb SNe

(Maurer et al. 2010; Jerkstrand et al. 2015; Ergon & Fransson 2022), Type Ic SNe (Mazzali et al. 2010), GRB/SNe, such as 1998bw (Mazzali et al. 2001; Dessart et al. 2017), or superluminous Type Ic SNe (Jerkstrand et al. 2017; Dessart 2019). But no systematic grid has ever been explored in detail for Type Ib and Ic SNe apart from D21. Indeed, these earlier simulations have often been one-zone models with no global and consistent connection to a progenitor and an explosion model, or they were based on single-star progenitor models whereas a binary progenitor channel was invoked. Binarity is probably essential for the production of Type Ib and Ic SNe (see, e.g., Wheeler & Levreault 1985; Ensman & Woosley 1988; Podsiadlowski et al. 1992), so employing binary-star progenitor models, together with their explosive result, appears mandatory in this context (see, e.g., Laplace et al. 2021). Here, we document the nebular-phase properties of a grid of He-star models covering the full range of masses for Type Ib and Ic SNe. These He-star models are thought to arise from binary mass transfer shortly after central helium ignition and thus implicitly require a binary progenitor (the subsequent evolution ignores any binary effect). Furthermore, we assume a solar metallicity and ignore rotation, so further work is needed to investigate the impact of these aspects on Type Ib and Ic SN observables.

In the next section, we briefly present the numerical setup for the present study. All details about the progenitor and explosion models as well as the radiative transfer approach are to be found in D21. In Sect. 3, we compare our results for two models of different initial mass but the same pre-SN mass and thus highlight some of the degeneracies of nebular-phase spectra. The photometric evolution for our grid of models is described in Sect. 4. We then discuss in detail and in turn our results for the main spectral landmarks of Type Ibc nebular spectra, namely, the emission lines [N II] $\lambda\lambda$ 6548, 6583, [O I] $\lambda\lambda$ 6300, 6364, [Ca II] $\lambda\lambda$ 7291, 7323, [Ni II] λ 7378, and the forest of Fe II lines below about 5500 Å. In Sect. 9, we discuss the implications of these results and present our conclusions. Comparisons to observations are deferred to Kuncarayakti et al. (in prep.). All model spectra are publicly available online[1].

2. Numerical setup

In this work, we continue and extend the radiative transfer modeling of He-star explosions presented in D21. Two sets of progenitor models are used. The first set corresponds to the He-star models of D21 with initial masses between 2.6 and 12.0 $M_\odot$ and evolved with a nominal mass loss rate (Yoon 2017). These were given the names he2p6, he2p9, ..., he12p0. This set is augmented with He-star models evolved without mass loss in order to consider progenitors in which the mass transfer phase leading to the H-rich envelope stripping occurs just before core collapse. Such models are suitable for progenitors leading to Type IIb SNe endowed with trace amounts of H-rich material[2]. To ensure moderate ejecta masses compatible with observations (see, e.g., Ensman & Woosley 1988 or Drout et al. 2011), we selected only a few masses in the range 2.5 to 4.5 $M_\odot$, spaced every 0.5 $M_\odot$. These models, evolved and exploded in the same fashion as the other set, are named he2p5MdZ etc – the suffix "MdZ" stands for MdotZero. This second set of models is used to assess the degeneracy of nebular phase spectra when determining yields or inferring the progenitor mass. As demonstrated below and already envisaged, the spectral properties are primarily dependent on the pre-SN mass, which depends on both the initial star mass and the uncertain wind mass loss. A summary of the ejecta properties for both model sets is provided in Table 1.

The second change relative to D21 is that all models are evolved from 100 to about 450 days, while only models he5p0, he6p0, and he8p0 were evolved (and only from 200 to 450 d) in D21. We thus provide a more extended nebular-phase evolution and for a wider range of He-star explosion models than currently available in the literature – this new set of simulations represents the largest grid of radiative transfer models for SNe Ibc at nebular times. Ideally, we would have evolved the models from a much earlier time (say 1 day after explosion), but the present simulations, which employ the shuffled-shell technique for macroscopic mixing (Dessart & Hillier 2020), require high resolution (with typically 350 radial points) and are thus extremely costly[3]. Furthermore, distinguishing between microscopic and macroscopic mixing during the photospheric phase is less critical because the plasma behaves similarly to a blackbody (i.e., a thermal emitter moderately influenced by line opacity and emissivity rather than a nebula cooled by lines). Chemical inhomogeneities and clumping nonetheless affect the SN radiation and gas properties (e.g., through a change in the radiative diffusion time) during the photospheric phase (Dessart et al. 2018; Dessart & Audit 2019; Ergon & Fransson 2022).

D21 presented an in-depth study of the radiative transfer at nebular times in Type Ib and Ic SN ejecta, but with a primary focus on a SN age of 200 days. Here, we compute the evolution at 20 epochs for 15 models, which corresponds to a total of 300 models. To avoid a lengthy presentation and repetition of results already presented in D21, the paper focuses on the evolution of key line diagnostics associated with the cooling of the four main ejecta shells (i.e., He, O, Si, or Fe rich), with only a brief description of the evolution of the optical spectra for a few representative models. The complete spectral evolution for the full set of models is presented in the appendix.

3. Properties of nebular phase spectra reflect primarily the pre-SN mass

The main stellar parameter sought for in nebular-phase spectroscopic modeling is the mass of the progenitor star on the main sequence. Oxygen is often used in this context as a diagnostic since its abundance is a rising function of He core mass in single star models (Woosley et al. 2002), and with final (i.e., pre-SN) mass in He-star models (Woosley 2019). This property has been extensively used to constrain the progenitor masses of Type II SNe (see, for example, Maguire et al. 2012; Jerkstrand et al. 2012; Silverman et al. 2017; Jacobson-Galán et al. 2022). The method has also been applied to stripped-envelope SNe but, as we demonstrate here, the method is flawed in SNe Ib and Ic because of pre-SN mass loss (SNe IIb are not affected because

[1] https://zenodo.org/communities/snrt

[2] At nebular times, this H-rich material is invisible (Jerkstrand et al. 2015; Ergon & Fransson 2022; D21), unless the ejecta interact with circumstellar material (Matheson et al. 2000; Dessart et al. 2023).

[3] The shuffled ejecta corresponding to models he2p6 to he12p0 used in this study are identical to those used in D21 – they are the same ejecta, only simulated over a different time span. The same procedure was applied to the unmixed ejecta models from progenitors evolved without mass loss. The approach in all cases was to split all shells (except the outermost shell) into three subshells and distribute them in the same order, starting from the innermost ejecta layer. We thus obtain a pattern of alternating shells of different composition repeated three times, connecting in the outer ejecta with the outermost shell that we excluded from the shuffling – see D21 for details and illustrations.

Table 1. Ejecta properties for our set of explosion models.

Model	$M_{\rm ZAMS}$ ($M_\odot$)	$M_{\rm preSN}$ ($M_\odot$)	$M_{\rm ej}$ ($M_\odot$)	$E_{\rm kin}$ [foe]	V_m [km s^{-1}]	^{4}He ($M_\odot$)	^{12}C ($M_\odot$)	^{14}N ($M_\odot$)	^{16}O ($M_\odot$)	^{24}Mg ($M_\odot$)	^{28}Si ($M_\odot$)	^{40}Ca ($M_\odot$)	^{56}Ni$_{t=0}$ ($M_\odot$)	^{58}Ni ($M_\odot$)
he2p6	13.85	2.15	0.79	0.13	4134	0.71	0.02	4.78(–3)	2.28(–2)	1.58(–3)	3.35(–3)	2.40(–4)	1.22(–2)	1.53(–3)
he2p9	14.82	2.37	0.93	0.37	6336	0.77	0.04	5.15(–3)	5.03(–2)	3.82(–3)	1.01(–2)	5.62(–4)	2.32(–2)	1.48(–3)
he3p3	16.07	2.67	1.20	0.55	6777	0.84	0.06	6.21(–3)	1.51(–1)	1.75(–2)	2.76(–2)	1.00(–3)	4.00(–2)	3.61(–3)
he3p5	16.67	2.81	1.27	0.41	5704	0.87	0.07	6.31(–3)	1.72(–1)	1.60(–2)	2.13(–2)	7.34(–4)	2.92(–2)	2.43(–3)
he4p0	18.11	3.16	1.62	0.63	6272	0.92	0.10	6.46(–3)	3.10(–1)	2.98(–2)	4.70(–2)	1.35(–3)	4.45(–2)	3.47(–3)
he4p5	19.50	3.49	1.89	1.17	7884	0.95	0.13	6.52(–3)	4.19(–1)	3.73(–2)	6.14(–2)	2.40(–3)	8.59(–2)	6.09(–3)
he5p0	20.82	3.81	2.21	1.51	8286	0.97	0.15	6.60(–3)	5.92(–1)	5.20(–2)	5.55(–2)	2.26(–3)	9.77(–2)	7.56(–3)
he6p0	23.33	4.44	2.82	1.10	6269	0.95	0.25	6.20(–3)	9.74(–1)	1.01(–1)	5.88(–2)	2.12(–3)	7.04(–2)	5.00(–3)
he7p0	25.68	5.04	3.33	1.38	6456	0.90	0.39	5.42(–3)	1.29(0)	1.07(–1)	9.47(–2)	3.42(–3)	1.02(–1)	4.19(–3)
he8p0	27.91	5.63	3.95	0.71	4251	0.84	0.49	5.17(–3)	1.71(0)	1.10(–1)	4.89(–2)	2.00(–3)	5.46(–2)	3.46(–3)
he12p0	35.74	7.24	5.32	0.81	3911	0.23	1.00	1.42(–4)	3.03(0)	8.73(–2)	7.41(–2)	3.42(–3)	7.90(–2)	2.47(–3)
he2p5MdZ	13.51	2.5	1.10	0.43	6237	0.87	0.05	4.08(–3)	9.20(–2)	3.41(–3)	1.33(–2)	8.39(–4)	3.48(–2)	2.58(–3)
he3p0MdZ	15.14	3.0	1.45	0.72	7077	0.98	0.08	7.12(–3)	2.07(–1)	1.29(–2)	3.82(–2)	2.25(–3)	5.64(–2)	2.51(–3)
he3p5MdZ	16.67	3.5	1.93	1.21	7941	1.06	0.10	7.34(–3)	4.26(–1)	4.25(–2)	7.14(–2)	3.57(–3)	1.02(–1)	5.02(–3)
he4p0MdZ	18.11	4.0	2.34	1.20	7168	1.11	0.13	7.45(–3)	6.71(–1)	5.88(–2)	8.93(–2)	4.53(–3)	1.07(–1)	4.75(–3)
he4p5MdZ	19.50	4.5	2.78	1.20	6573	1.15	0.16	6.60(–3)	9.62(–1)	7.91(–2)	9.27(–2)	4.33(–3)	1.01(–1)	4.44(–3)

Notes. The upper part describes the models already used in D21 while the lower part describes new models arising from progenitors evolved without wind mass loss. The table columns correspond to the ZAMS mass, the preSN mass, the ejecta mass, the ejecta kinetic energy (1 foe $\equiv 10^{51}$ erg), the mean expansion rate $V_{\rm m} \equiv \sqrt{2E_{\rm kin}/M_{\rm ej}}$, the cumulative yields of ^{4}He, ^{12}C, ^{14}N, ^{16}O, ^{24}Mg, ^{28}Si, ^{40}Ca, ^{56}Ni prior to decay, and ^{58}Ni. All ^{56}Ni masses used here were taken from the KEPLER approximation to the P-HOTB neutrino simulation (see discussion in D21).

mass-loss has left a small residual H-rich envelope, and hence an intact He core in the progenitor at core collapse).

D21 showed the close correspondence between the O mass and the pre-SN mass (for H-deficient stars) or the He-core mass (for H-rich stars) for a wide range of binary-star and single-star models. Using the O yield to infer the original, main sequence mass of H-deficient stars is, however, difficult because of the influence of mass loss on the bare He core once the H-rich envelope is gone. This uncertain impact of mass loss compromises any robust determination of the initial mass of Type Ib and Ic progenitors – we may only set a lower bound on the initial mass and infer their pre-SN mass from nebular-phase observations.

This issue with mass loss does not affect Type II and IIb SNe since their He core remains enshrouded throughout the progenitor life. In addition to these considerations, the O yield may be further affected by the processes of convection, semi-convection, overshoot, or rotation, for which we lack a robust theory (e.g., convection) or good observational constraints (e.g., rotation).

As we demonstrate in the following discussion, our two sets of models with and without mass loss teach us a number of important lessons. First, the models confirm the good correlation between O-yield and pre-SN mass (Table 1, and particularly Table 2; see also Sect. 3 and Fig. 3 in D21). Second, the composition structure of models with the same pre-SN mass exhibits subtle differences – different shells have different mass and exhibit different compositions. Third, different progenitor masses on the He zero-age main sequence can lead to similar nebular spectra. Fourth, while the [O I] $\lambda\lambda$ 6300, 6364 line strength may provide a robust indication of the O yield, its connection to the initial mass of the progenitor on the H or He zero age main sequence is more tenuous.

Figure 1 shows the unmixed composition (i.e., prior to the shell shuffling used to enforce some macroscopic mixing) for models he4p5MdZ and he6p0. While the pre-SN mass and O-yield are identical within a few percent, model he4p5MdZ has a bigger O/Si shell, a smaller O/Ne/Mg shell, a bigger O/C shell, and its He/C shell has a lower C and O mass fraction than in the model he6p0. Inferring such subtle differences from nebular phase spectroscopy is probably impossible, in part because macroscopic mixing transforms this clean shell structure into a complicated 3D structure. The mass range occupied by the O-rich shell (~0.2 to ~1.7 $M_\odot$ above the innermost ejecta layer at 1.6–1.7 $M_\odot$) and the He-rich shell (the layers above the O-rich shell) is nonetheless comparable in both models. Finally, the core structure differs. Although the mass cut in model he4p5MdZ was located further out (1.71 instead of 1.60 $M_\odot$ in model he6p0), its compactness and its explosion energy are greater ($E_{\rm kin}$ = 1.2 foe instead of 1.1 foe), causing a more extensive explosive nucleosynthesis (0.1 versus 0.07 $M_\odot$ – a greater ^{56}Ni mass is also found in other MdZ models relative to He star models evolved with mass loss and having the same pre-SN mass; see Table 1).

The differences in composition structure can be explained. Despite the similar final mass, the models he6p0 and he4p5MdZ are different stars with different evolutionary histories. In the

Table 2. Comparison of oxygen yields.

Model	$M_{\rm pre-SN}$ ($M_\odot$)	O yield ($M_\odot$)
he2p9	2.37	0.05
he2p5dZ	2.50	0.092
he3p3	2.67	0.15
he4p0	3.16	0.31
he3p0MdZ	3.00	0.21
he3p5MdZ	3.50	0.43
he4p5	3.49	0.42
he5p0	3.81	0.59
he4p5MdZ	4.50	0.96
he6p0	4.44	0.97

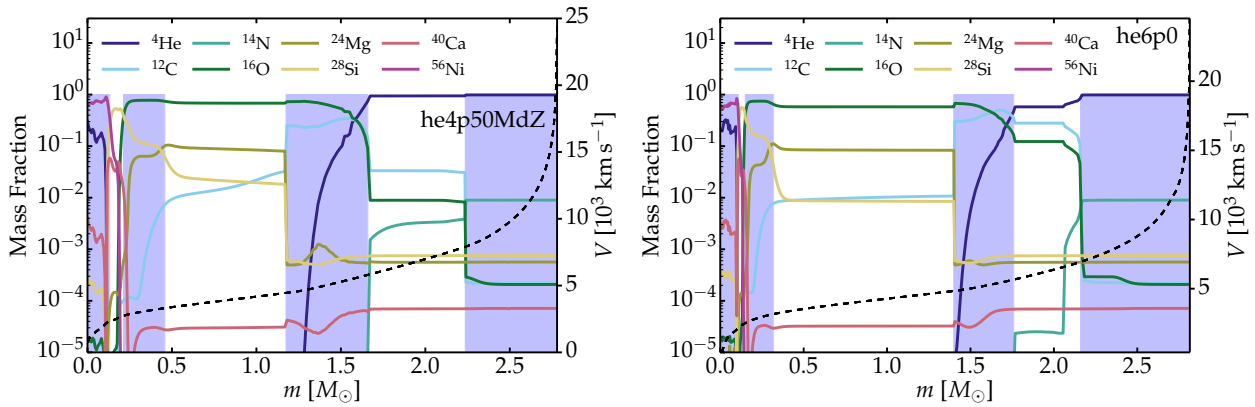

Fig. 1. Comparison of the he4p5MdZ (left: $M_{\rm preSN} = 4.5\,M_\odot$) and he6p0 (right: $M_{\rm preSN} = 4.44\,M_\odot$) unmixed ejecta models. The alternating shades of blue and white indicate the successive shells in the original unmixed ejecta. Starting from the innermost ejecta layer, one progresses outwards through the Fe/He, Si/S, O/Si, O/Ne/Mg, O/C, He/C, and He/N shells.

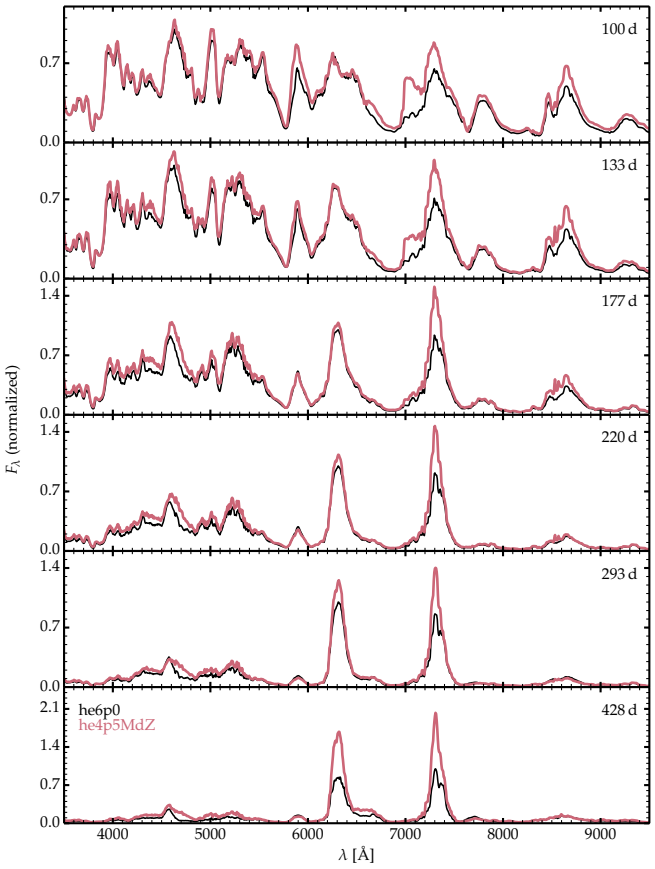

Fig. 2. Comparison of multi-epoch optical spectra for models he6p0 (black; with nominal mass loss) and he4p5MdZ (red; progenitor evolved with no mass loss) from 100 to 428 days after explosion. At each epoch, the same normalization is applied to both spectra.

absence of wind mass loss (model he4p5MdZ), the mass stays fixed during helium burning and the convective core extends out to some point appropriate to that mass and stays there. However, when wind mass loss operates, the star mass shrinks and the helium convective core recedes accordingly. The resulting entropy profile and location of burning shells, in particular, the helium burning shell, are altered. The relatively modest differences in final composition profiles suggest that the mass lost was not a large fraction of the initial mass. Furthermore, the difference in explosion properties reflects the differences in their pre-SN core structure. For example, the radius encompassing $2.5\,M_\odot$ in he4p5MdZ is 1.56×10^9 cm. For he6p0, it is 2.58×10^9 cm. This results in different efficiencies of the explosion engine.

Figure 2 compares the CMFGEN spectra of model he4p5MdZ and he6p0 at multiple epochs spanning the range 100 to 428 days. Despite the different progenitor masses on the He zero-age main sequence, the similarities in the ejecta composition, mass, and kinetic energy lead to very similar spectra at all epochs. Some differences are, however, noticeable at certain epochs and locations. More power is absorbed in the more He-pure He-rich shell of model he4p5MdZ (Fig. 1), which leads to stronger He I lines at 100 and 133 days – no obvious He I line is present at later times in the optical range. Furthermore, the greater ^{56}Ni mass in model he4p5MdZ (0.1 versus $0.07\,M_\odot$) leads to a stronger [Ca II] $\lambda\lambda$ 7291, 7323 since this is the main coolant of the Fe/He and Si/S shells (D21; both shells are bigger in model he4p5MdZ; see left column of Fig. 1). This emphasizes that the ratio of emission fluxes associated with [O I] $\lambda\lambda$ 6300, 6364 and [Ca II] $\lambda\lambda$ 7291, 7323 is not a straightforward progenitor mass diagnostic – the O yield scales with the pre-SN mass and pre-SN nucleosynthesis while the [Ca II] $\lambda\lambda$ 7291, 7323 line strength scales with the amount of explosively nucleosynthesized material, which depends on numerous progenitor characteristics other than pre-SN mass (i.e., compactness, explosion energy, or mass cut).

At the latest epoch, model he4p5MdZ shows much stronger [O I] $\lambda\lambda$ 6300, 6364 and [Ca II] $\lambda\lambda$ 7291, 7323 line emission than model he6p0. The relative fraction of power absorbed in the various shells is very similar in both models but because of its greater ^{56}Ni mass, all powers are scaled up by ~50% in model he4p5MdZ, so that line fluxes are also ~50% stronger in model he4p5MdZ. Renormalizing the spectra so that both models have the same decay-power absorbed reduces the offset between the model spectra but some offset remains. This can be explained by differences in composition and ionization. For example, model he4p5MdZ has a higher $E_{\rm kin}/M_{\rm ej}$, which leads to a slightly higher ionization in the O-rich shell – the more recombined O-rich material in the he6p0 model cools in part through Na I $\lambda\lambda$ 5896, 5890, causing a reduction in the flux of [O I] $\lambda\lambda$ 6300, 6364. This shows the complexity of inferring ejecta properties and composition from nebular-phase spectra, even in a controlled experiment based on two very similar ejecta models.

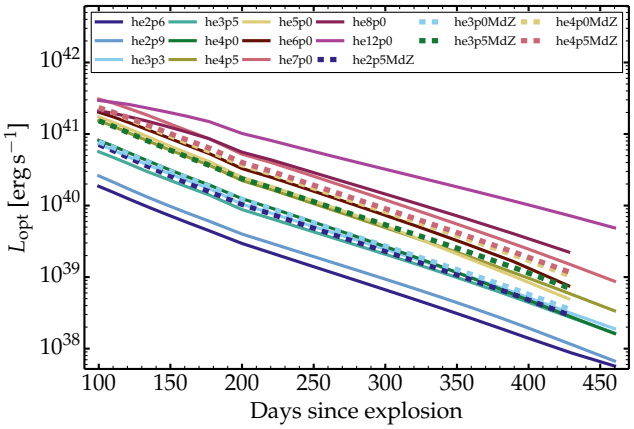

Fig. 3. Evolution of the optical luminosity for our set of He-star explosion models evolved with and without mass loss. At 100 days the models vary in flux by over an order of magnitude, while at 450 days, the variation in optical flux is nearly two orders of magnitude.

To conclude, this comparison emphasizes that while the [O I] $\lambda\lambda$ 6300, 6364 line strength may provide a robust indication of the O yield, the connection to the initial mass (whether that is the H or the He zero age main sequence) cannot be established precisely. Only a range of progenitor masses may be inferred based on various assumptions concerning the pre-SN mass loss history. It also shows that one may produce a variety of progenitor models for a given nebular-phase spectrum (the present comparison also ignores any departure from spherical symmetry or the effect of clumping).

4. Photometric evolution

Figure 3 shows the evolution of the optical luminosity (corresponding to wavelengths between 3500 and 9500 Å) from 100 to about 450 days after explosion for the full set of models. The evolution of the bolometric luminosity and the fraction of that power falling in the UV (wavelengths below 3500 Å), optical, and IR (wavelengths beyond 9500 Å) ranges is shown in Fig. A.1.

As for SNe II at nebular epochs (Dessart et al. 2021b), these He-star explosion models radiate about 70% of their luminosity in the optical range (it is about 10% in the UV, and about 20% in the IR; Fig. A.1). Relative to Type II SN models of different masses (Dessart et al. 2021b), there is a much greater scatter here. Lower mass progenitors, because of their greater He content, are systematically bluer, with more flux emerging in the UV (up to 15% for model he2p6) and less in the optical and IR. Higher mass models (especially he8p0 and he12p0) are cooler and more recombined and exhibit their strongest lines in the optical where they radiate up to 80% of their total flux with just a few percent falling in the UV.

This relative constant distribution of the SN luminosity between UV, optical, and IR ranges occurs despite the drop in bolometric luminosity by a factor of 50 to 100 between 100 and 450 days. As already discussed in D21, γ-ray leakage progressively increases and modulates the relative contribution from positrons, which we assume are absorbed locally (Fig. A.2). In model he12p0, there is nearly full γ-ray trapping at 100 days but only 30% trapping at 450 days. At the opposite end of the mass range, model he2p9 traps 30% of emitted γ rays at 100 days. For all light models, the fractional decay power absorbed at 450 days is 6–10%, with therefore as much as 50% of the total decay power coming from positrons. In such models, this implies that 50% of the emission originates from the ejecta regions rich in ^{56}Ni initially.

5. Spectral evolution for four He-star progenitor masses

The He-star explosion models discussed in D21 reveal a wide range of nebular-phase spectral properties. At 200 days after explosion, we identified three different families with prototypes of the he3p3, the he5p0, and the he8p0 models. These distinct models also exhibit different evolutions from 100 to 450 days. To avoid duplication with D21 and to cover more finely the differences between models, we show in Fig. 4 the optical spectral evolution for models he2p6, he4p0, he6p0, and he8p0. This figure also details the contributions from bound-bound transitions associated with He I, N II, O I, Na I, Mg I, Ca II, "iron," (i.e., the synthetic spectrum computed with a formal solution includes simultaneously Fe I, Fe II, and Fe III bound-bound transitions) and Ni II. In each model, similar lines are seen at all epochs but their strengths varies greatly in time. In this section, we present the main spectral characteristics and defer to the following sections their interpretation (see also D21).

Model he2p6 (top left panel of Fig. 4) is at the low-mass end of our model set and exhibits spectral properties unlike that typically observed for Type Ib and Ic SNe. At 100 days, the spectrum exhibits strong He I recombination lines at 5875, 6678, 7065 Å, [N II] λ 5755 and [N II] $\lambda\lambda$ 6548, 6583, a few O I lines including weak [O I] $\lambda\lambda$ 6300, 6364, Na I $\lambda\lambda$ 5896, 5890 (which overlaps with He I 5875 Å), Ca II lines with the [Ca II] $\lambda\lambda$ 7291, 7323 doublet (which merges into a single broad feature with the adjacent emission from [Ni II] λ 7378), and finally an extended Fe emission (primarily due to Fe II) between 4000 and 5500 Å. As time passes, the He I lines weaken (He I 6678 Å soon vanishes but the lines at 5875 and 7068 persist throughout the evolution). [N II] λ 5755 weakens while [N II] $\lambda\lambda$ 6548, 6583 strengthens and becomes the strongest line in the optical range at $\gtrsim$400 days. Na I $\lambda\lambda$ 5896, 5890 eventually becomes the primary contributor to the 5900 Å emission feature. At most epochs, the [Ca II] $\lambda\lambda$ 7291, 7323 doublet is strong except at the earliest and latest epochs. Iron emission abates a little in the course of the evolution but remains quite strong.

Model he4p0 (top right panel of Fig. 4) shares a number of properties with model he2p6 but the iron emission is much weaker after about 200 days, the [N II] $\lambda\lambda$ 6548, 6583 doublet (with a broad and boxy profile) follows a similar evolution but never becomes as strong, the [O I] $\lambda\lambda$ 6300, 6364 doublet is much stronger, the [Ca II] $\lambda\lambda$ 7291, 7323 is strong at all times (here with a smaller contribution from [Ni II] λ 7378) and stronger than [O I] $\lambda\lambda$ 6300, 6364 at all times. Mg I] λ 4571 is now predicted at most epochs but invisible before about 400 days, in part because of blanketing by overlapping Fe II transitions. The Ca II $\lambda\lambda$ 8498 – 8662 is quite strong initially but vanishes after about 200 days.

Model he6p0 (bottom left panel of Fig. 4) is analogous to model he4p0, but shows a stronger [O I] $\lambda\lambda$ 6300, 6364 at all times, which now rivals in strength with the [Ca II] $\lambda\lambda$ 7291, 7323 doublet, while the [N II] $\lambda\lambda$ 6548, 6583 is now much weaker and hard to distinguish. The iron emission is strong from 100 to 200 days but progressively weakens until the last epoch. In model he6p0, Na I $\lambda\lambda$ 5896, 5890 is the sole contributor to the 5900 Å feature except at the earliest epochs.

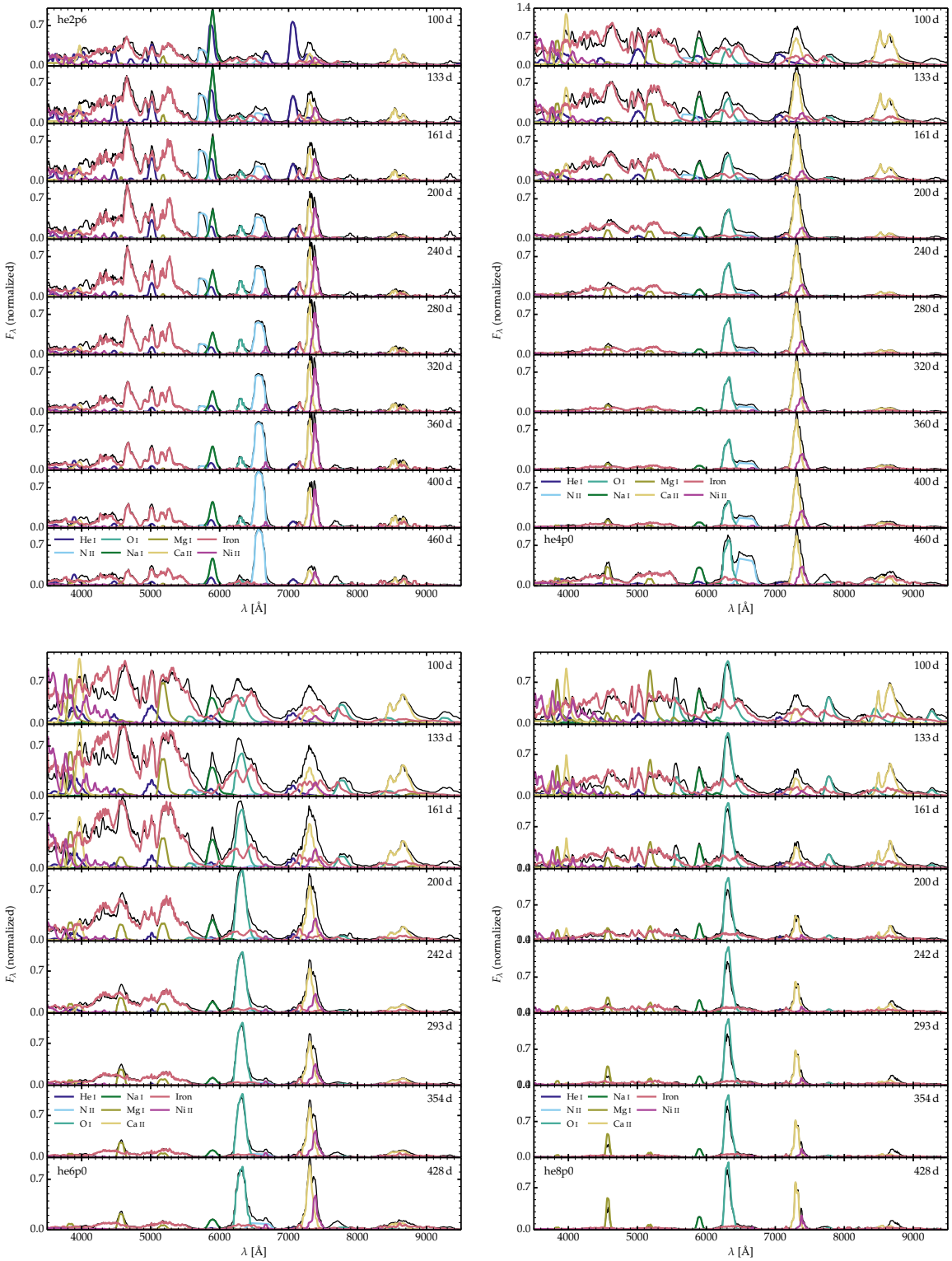

Fig. 4. Evolution of the optical spectrum of models he2p6 (top left), he4p0 (top right), he6p0 (bottom left), and he8p0 (bottom right) from 100 to about 450 days (black). Also plotted is the contribution from bound-bound transitions associated with various ions ("iron" corresponds to a simulation of the spectrum that includes all Fe I, Fe II, and Fe III bound-bound transitions) – these individual contributions dominate in turn in distinct spectral regions so that the black line giving the total flux, which is exclusively an emission line spectrum, is hardly visible at any epoch. [N II] $\lambda\lambda$ 6548, 6583 dominates the emission near 6500 Å in he2p6, is present in he4p0 at later epochs, but absent in the higher pre-SN mass models. In the latter two models, [O I] $\lambda\lambda$ 6300, 6364 is the prominent feature near 6300 Å.

Model he8p0 (see bottom-right panel of Fig. 4) shows a weaker iron emission than all other models, and this iron emission eventually vanishes at late times when the model cools primarily through Mg I] λ 4571, Na I $\lambda\lambda$ 5896, 5890, [O I] $\lambda\lambda$ 6300, 6364, and [Ca II] $\lambda\lambda$ 7291, 7323. As in model he6p0, the O I $\lambda\lambda$ 7771 – 7775 line is strong at early times.

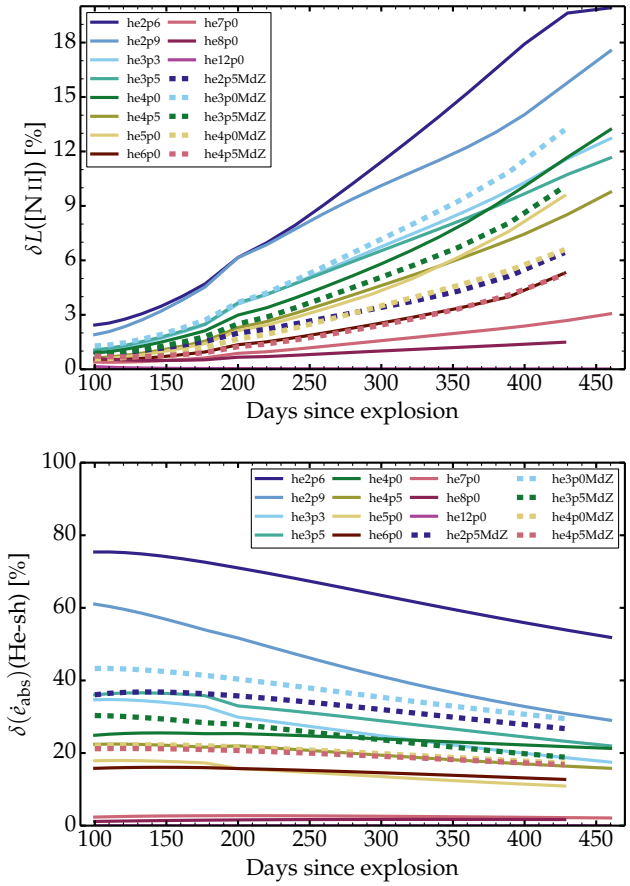

Fig. 5. Evolution of important powers associated with the He-rich shell in our sample of He-star explosion models. Top: Fractional line flux in [N II] $\lambda\lambda$ 6548, 6583 relative to the total optical luminosity versus time since explosion for our radiative-transfer calculations based on the ejecta models he2p6 to he12p0 arising from He-star progenitors evolved with the nominal mass loss rate (Woosley 2019; Ertl et al. 2020, solid line) and on the ejecta models he2p5MdZ to he4p5MdZ arising from He-star progenitors evolved with no mass loss (dashed line). Bottom: Same as above but showing the fraction of the total decay power absorbed in the He-rich shell. Both are given as a percentage.

Apart from the earlier epochs with Fe II emission, the spectrum changes little beyond 200 days. Of these four models, he8p0 shows the strongest [O I] $\lambda\lambda$ 6300, 6364, which is also the strongest emission in the optical at all times between 100 and 428 days. We also note that in all models after about 400 days, the resonance transition K I $\lambda\lambda$ 7665, 7699 strengthens – we note that this should not be confused with the blueshifted emission from O I $\lambda\lambda$ 7771 – 7775.

A complementary comparison of spectral properties is presented in Fig. A.3 where we compare all the models (He-star progenitors evolved with a nominal mass loss) at 100, 200, 320, and 430 days after explosion. In the next sections, we discuss in turn the strongest lines that represent landmarks in at least one model in our set. We start with [N II] $\lambda\lambda$ 6548, 6583 (Sect. 6), followed by [O I] $\lambda\lambda$ 6300, 6364, and Mg I] λ 4571 (Sect. 7). Finally, we discuss the Ca II, Ni II, and Fe II lines (Sect. 8).

6. The He-rich shell and [N II] $\lambda\lambda$ 6548, 6583

Figure 5 shows the percentage of the optical flux (i.e., within 3500 and 9500 Å) radiated in [N II] $\lambda\lambda$ 6548, 6583 as a function of time for the full set of models. The integration of the line flux extends out to $\pm 12\,000$ km s^{-1} from the mean rest wavelength of the doublet (taken at 6565.5 Å) and hence the reported flux accounts for the contribution of both components. Because this doublet forms in the He/N shell, we also show the evolution of the power absorbed in the He-rich shell as a function of time (bottom panel).

This fractional flux is only a few percent at 100 days but grows to 2–20% at 450 days. This increase is caused by various factors. The density drops as $1/t^3$ (where t is the elapsed time since explosion) and eventually favors cooling through forbidden lines. N is primarily once ionized, favoring a high population of the N II ground state (see Figs. A.4–A.5 for additional information on the ionization and temperature in all ejecta shells). Finally, the [N II] $\lambda\lambda$ 6548, 6583 doublet is eventually the dominant coolant for the He/N shell, swamping the cooling due to Fe II. The strength of [N II] $\lambda\lambda$ 6548, 6583 varies between models because of the difference in decay power absorbed in that shell, which itself scales with the He/N shell mass. Model he2p6 (he8p0) is endowed with a He-rich shell that represents 92% (15%) of the ejecta mass and absorbs a fraction of the total decay power that is 75% (1%) at 100 days but only 52% (2%) at 450 days.

The temporal evolution of the decay power absorbed in the He-rich shell does not just depend on the mass of the He-rich shell. In model he2p6, the γ-ray escape from the ejecta is large so positron deposition increasingly dominates the total decay power absorbed (it represents 37% at 450 days in this model). This power provides little benefit to the He-rich shell because it is ^{56}Ni free, and hence the fraction of energy emitted by the He-rich shell declines with time. However, [N II] $\lambda\lambda$ 6548, 6583 remains prominent since it radiates a larger fraction of the energy deposited in the He-rich shell. In higher mass models, the γ-ray trapping is greater so positron power plays a weaker role (see also Fig. A.2). In that case, with time passing, γ rays can travel some distance before being absorbed or escaping. In models more massive than he4p0, the power absorbed in the He-rich shell stays essentially constant with time.

7. The O-rich shell and [O I] $\lambda\lambda$ 6300, 6364

Figure 6 shows the percentage of the optical flux radiated in [O I] $\lambda\lambda$ 6300, 6364 (top panel) and Mg I] λ 4571 (middle panel), as well as the fraction of the total decay power absorbed in the O-rich shell (bottom panel) as a function of time for all He-star explosion models (progenitors evolved with and without mass loss). Both fractional line fluxes increase with time but they seem to reach a maximum at about 300 days for [O I] $\lambda\lambda$ 6300, 6364 and 400 days for Mg I] λ 4571. Instead, the decay power absorbed in the O-rich shell decreases steadily in all models at all times except for models he8p0 and he12p0 for which there is first a rise from 100 to 200 days and then a slow decrease.

In lower mass ejecta, the lower O yield and the lower O-rich shell mass lead to a weaker [O I] $\lambda\lambda$ 6300, 6364. The progressive recombination of O contributes to strengthening [O I] $\lambda\lambda$ 6300, 6364 with time. In higher mass models, the O ionization is always low so recombination in time mostly contributes to decreasing the [O I] $\lambda\lambda$ 6300, 6364 and strengthening Mg I] λ 4571 at times past 300 days. In model he12p0, the [O I] $\lambda\lambda$ 6300, 6364 flux represents 10% of the optical flux at 100 days, but 40% at 350 days. In low-mass models, the [O I] $\lambda\lambda$ 6300, 6364 flux is just a few percent of the optical flux and always remains subdominant. The evolution of Mg I] λ 4571 is qualitatively similar to that of [O I] $\lambda\lambda$ 6300, 6364 but shifted

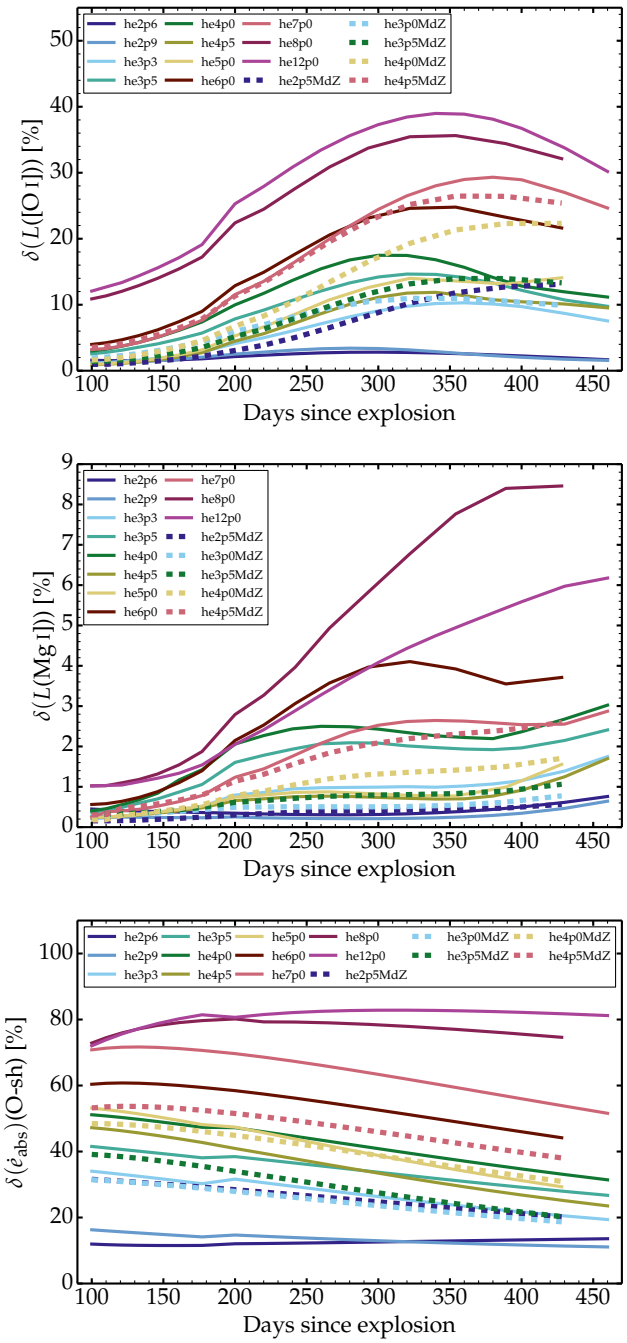

Fig. 6. Same as Fig. 5, but showing the fractional flux associated with [O I] $\lambda\lambda$ 6300, 6364 (top panel) and Mg I] λ 4571 (middle panel), as well as the fractional decay power absorbed in the O-rich shell (bottom panel).

to smaller line fluxes because of the lower Mg abundance (see Table 1). The delayed rise and peak stems from an ionization effect since Mg stays partially ionized for longer (the ionization potential of Mg I is 7.6 eV while that of O I is 13.6 eV). A similar effect occurs for Na I, which also has a small ionization potential (i.e., 5.1 eV) and Na I $\lambda\lambda$ 5896, 5890 strengthens only later on. In model he12p0 (or he8p0), the drop in [O I] $\lambda\lambda$ 6300, 6364 flux after 350 days is due to an increased leakage of power into Mg I] λ 4571 and Na I $\lambda\lambda$ 5896, 5890.

In high-mass progenitors, the O-rich shell represents the bulk of the ejecta mass (97% in model he12p0) and captures the bulk of the decay power. The [O I] $\lambda\lambda$ 6300, 6364 is not strong early on because the density is too high (which inhibits forbidden line formation) – there is little change in terms of the O ionization in the O-rich shell in that model. In lower mass models, the O-rich shell is smaller (it represents 45% of the total mass in model he5p0) and absorbs less power, but the O ionization is partial so a fraction of that power is radiated by Fe II lines. Both effects conspire to reduce the [O I] $\lambda\lambda$ 6300, 6364 line strength and benefit Fe II line emission, particularly at early times. But the progressive cooling leads to the strengthening of both [O I] $\lambda\lambda$ 6300, 6364 and Mg I] λ 4571.

Clumping can impact the strength of [O I] $\lambda\lambda$ 6300, 6364 in models that exhibit a partial O ionization (D21) at any epoch. Clumping does not boost the strength of the emission directly, but instead indirectly through the recombination it induces. D21 found that a modest compression of the O-rich material can enhance the population of neutral O, which eventually takes place in most models at 300–400 days. Uncertainties in clumping are thus less impactful at late times, making them more suitable to infer the yields from SNe Ib and Ic in that respect. Unfortunately, molecule and dust are likely to start forming at these times (see, e.g., Jerkstrand et al. 2015; Rho et al. 2021). Since the effects of clumping have been documented in detail in D21, they are not repeated here.

8. The Fe/He and Si/S shells and Ca II, Ni II, and Fe II lines

Figure 7 shows some important diagnostics for the Si-rich and Fe-rich shells. Both shells were grouped here for simplicity because they are thin and hard to distinguish in our models. Furthermore, their composition is in fact similar in many ways, with Ca and ^{56}Ni abundant in both shells (D21). Figure 7 shows the evolution of the fraction of the optical flux emerging in [Ca II] $\lambda\lambda$ 7291, 7323 (top left panel), in Ca II $\lambda\lambda$ 8498 – 8662 (top right panel), in the iron lines (middle left panel), in [Ni II] λ 7378 (middle right panel), as well as the fraction of the total decay power absorbed in the combined Si-rich and Fe-rich shells (bottom row panel), for all He-star explosion models (progenitors evolved with and without mass loss). While Ca is most abundant in the Si-rich shell, the [Ca II] $\lambda\lambda$ 7291, 7323 forms both in the Fe-rich and the Si-rich shells and the Ca II $\lambda\lambda$ 8498 – 8662 may form everywhere, including in the O-rich shell where its abundance is subsolar (see D21 for discussion).

Because the Ca-rich layers are formed through explosive burning, the Ca abundance scales with the ^{56}Ni mass and is thus not an ideal diagnostic of the pre-SN mass (unlike O). In our set of models, the ^{56}Ni mass is between 0.01 and 0.1 $M_\odot$, with a lot of scatter between models although there is a tendency for small values at the low mass end (the minimum ^{56}Ni mass of 0.01 $M_\odot$ is for the lightest model in the sample, i.e., he2p6). The [Ca II] $\lambda\lambda$ 7291, 7323 doublet line strength is seen to rise in all models until about 350 days. This rise stems in part from the drop in density and in ionization, and mirrors the drop in iron line emission. In lower-mass models, this rise stems also from the fact that the decay power absorbed in the combined Si-rich and Fe-rich shells increases in time following the growing fraction of local energy deposition from positrons while γ rays increasingly escape the ejecta (and deprive the O-rich and He-rich shells).

The apparent strength of the 7300 Å feature in our spectra comes in part from [Ni II] λ 7378. Stable Ni (i.e., ^{58}Ni) is present with a mass between about 0.001 and 0.008 $M_\odot$. In the model most abundant in ^{58}Ni (namely he5p0), the [Ni II] λ 7378 line flux represents ~1% of the total optical flux at 100 days but this

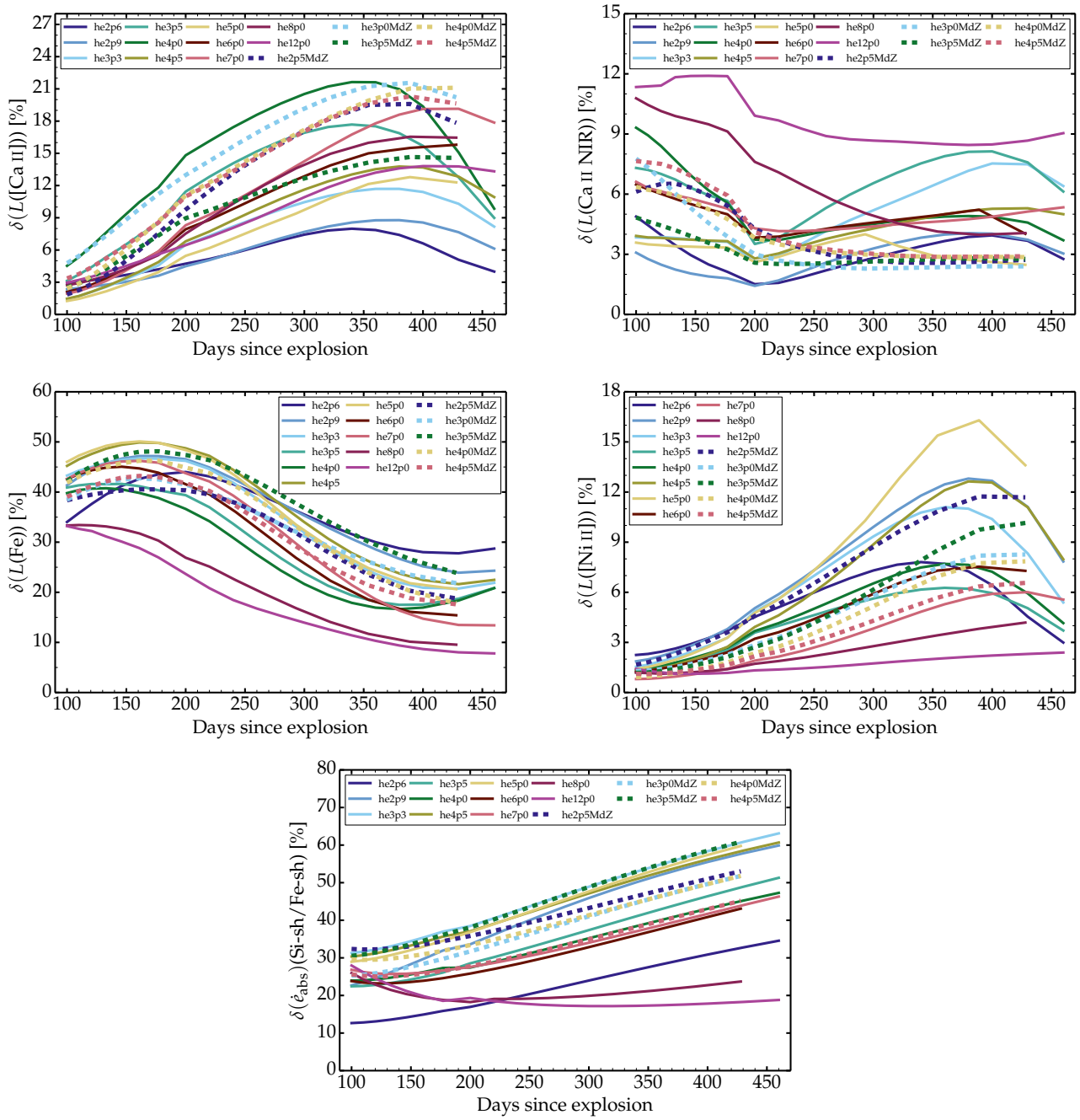

Fig. 7. Same as Fig. 5, but showing the fractional flux associated with [Ca II] $\lambda\lambda$ 7291, 7323 (top left panel), with Ca II $\lambda\lambda$ 8498 − 8662 (top right panel), with Fe emission in the 4100–5500 Å range (middle left panel), and with [Ni II] λ 7378 (middle right panel), as well as the fractional decay power absorbed in the combined Si-rich and Fe-rich shells (bottom panel).

fraction rises to ∼15% at 400 days. Not knowing a priori the abundance of ^{58}Ni in any observed SN (in the infrared, the less blended [Ni II] lines at 1.94 and 6.63 µm might help reduce this uncertainty), it is unclear what fraction of the 7300 Å line flux is due to [Ca II] $\lambda\lambda$ 7291, 7323. This emission at 7300 Å should therefore be used with caution in any mass estimate.

The iron emission in the range 4000–5500 Å represents a significant fraction of the SN radiation at 100 days in all models, and this persists at all times covered here in lower mass models. Fe II emission occurs not just in the Fe/He shell but throughout the ejecta. Partial ionization at early times (which prevents strong forbidden lines like [O I] $\lambda\lambda$ 6300, 6364 to form) favor Fe II cooling in the O-rich shell. In lower mass He-star models, Fe II is an important coolant of He-rich material (in addition to N II). In the O-rich shell, Fe II cooling tends to persist as long as ejecta densities are too high for the formation of forbidden lines (these appear when radiative de-excitation is more likely than collisional de-excitation).

9. Discussion and conclusions

We present a grid of time-dependent non-LTE radiative transfer simulations computed with `CMFGEN`, covering the nebular phase from 100 until about 450 days after explosion, and based on He-star progenitor and explosion models originally computed by Woosley (2019) and Ertl et al. (2020). This study is an

extension of our previous work (D21) based on similar models, where we focused on the properties at a single epoch of 200 days after explosion. These calculations currently represent the largest grid of radiative transfer models for SNe Ibc at nebular epochs. Despite the large number of models, we ignored the possibility of clumping, molecule formation, or departures from spherical symmetry so that this model grid underestimates the real extent of the parameter space covered by SNe Ib and Ic as well as the degeneracy of their radiative properties. To maintain concision, this presentation was limited to model results. Details about the underlying ejecta properties or the complications of line formation in SNe Ibc were presented in D21. A comparison of the present models, together with those discussed in D21, with the observations of Type Ib and Ic SNe will be presented elsewhere.

As discussed in D21, the pre-SN yields of He-star models depend on pre-SN mass loss, such that He stars dying with the same final mass have a comparable O yield (or CO core mass). This implies that evaluating the nucleosynthesis of SN Ibc ejecta can (at best) constrain the pre-SN mass but not the original mass on the main sequence. It also implies that Type Ibc progenitors of a given mass on the main sequence will tend to contribute lesser proportions of metal at a higher metallicity. To address this aspect and quantify its impact, we computed a new set of models in which no pre-SN mass loss was assumed. While our He-star models likely result from the early removal of the H-rich envelope in an interacting binary at the onset of He-core burning, these zero mass loss models correspond to a similar removal taking place just before core collapse. The two sets of models probably bracket the range of possibilities for the timing of the envelope removal as well as uncertainties in wind mass loss rate. To keep in line with the low ejecta masses inferred from observations of SNe Ibc, we limit this set of zero mass loss models to low initial He-star masses (i.e., 2.5–4.5 $M_{\odot}$), yielding ejecta masses in the range of 1.1–2.8 $M_{\odot}$.

In this comparison, we showed that models he4p5MdZ and he6p0 – which die with a final mass of 4.5 and 4.44 $M_{\odot}$, and He mass of 1.15 and 0.95 $M_{\odot}$, and an O mass of 0.97 and 0.96 $M_{\odot}$ – produce similar spectra over the 100 to 450 days timespan. Models with the same final, pre-SN mass have similar yields and produce essentially the same emergent spectra, and only weak and transitory differences are apparent. He I 7065 Å is stronger prior to ∼150 days in model he4p5MdZ. The 40% greater ^{56}Ni mass in that model yields a greater brightness and is also likely at the origin of the slightly stronger [Ca II] $\lambda\lambda$ 7291, 7323 since that line forms in the Fe/He and Si/S shells, which are both explosively produced. Numerous finer differences in these two ejecta and progenitor models, including different O/Ne/Mg and He/C shell masses, the C and O mass fraction in the He/C shell, or the different $E_{\rm kin}/M_{\rm ej}$, are hard to diagnose and suggest a further degeneracy of nebular-phase spectra. The uncertain progenitor mass loss history thus compromises the inference of the initial, main sequence mass of SNe Ib and Ic. We note that this shortcoming does not affect SNe IIb whose progenitor He core is intact at the time of core collapse.

Our broad set of models from low-mass to high-mass He star progenitors yield SN Ibc spectra with large differences at all epochs. That is to say, models that differ significantly in pre-SN mass have widely different spectral properties at any given time of the nebular evolution. These differences reflect the different masses of the Fe/He, Si/S, O-rich (i.e., O/Si, O/Ne/Mg and O/C), and He-rich (i.e., He/C and He/N) shells and the fact that the power absorbed in a shell scales to first order with its mass. Hence, at the low He-star mass end, the pre-SN models have a composition dominated by the He-rich shell with small metal yields. Such models exhibit strong Fe II emission in the 4000–5500 Å range (this emission is always stronger early on) and weak [O I] $\lambda\lambda$ 6300, 6364 at all times. He I lines are present up until about 150 days, while N II lines are present at all nebular epochs, with [N II] $\lambda\lambda$ 6548, 6583 even becoming the strongest optical line at 450 days.

Higher mass models, characterized by a decreasing He-rich shell mass and an increasing O-rich shell mass, show weaker emission from the He-rich shell (weak or no He I and N II lines), while the emission from the O-rich shell strengthens. At early times, and in the absence of clumping, O is partially ionized in lower mass He-star models so a fraction of the O-rich shell cools through Fe II emission. However, after about 300 days, O is essentially neutral in the O-rich shell and the [O I] $\lambda\lambda$ 6300, 6364 is strong, and this is all the more true for larger He-star models. The [Ca II] $\lambda\lambda$ 7291, 7323 emission is a poor tracer of the pre-SN mass because its strength scales with the Fe/He and Si/S shell masses, which result from explosive nucleosynthesis.

Quantifying the nucleosynthetic yields and characterizing the progenitors of Type Ibc SNe from nebular phase spectra seems easier at times later than 300 days. At such late times, the ejecta cool through a few strong lines rather than a myriad of lines. Furthermore, the ionization in the O-rich shell is predicted to be low (O is essentially neutral), even in the absence of clumping. Hence, the uncertain level of clumping is less critical. However, at these epochs cooling by CO and other molecules is likely to be important, and will need to be considered in future models.

More quantitative information can be gleaned by studying the evolution of line fluxes through the nebular phase (as done here from 100 to 450 days), rather than focusing on one or two epochs. Indeed, the full evolution reveals the change in temperature or ionization of ejecta shells of different composition, the evolving power contribution of γ-rays and positrons etc. As we argue in Dessart et al. (2022b), the *Vera C. Rubin* Observatory Legacy Survey of Space and Time will provide important information on the photometric evolution of a large sample of SNe Ibc, which will complement what has been achieved so far primarily with spectroscopy.

Inferring the mass of ^{56}Ni from SN Ibc nebular spectra is challenging. This may be done in SNe Ia because the ^{56}Ni mass is typically half the ejecta mass and the ionization is relatively high. This allows for the simultaneous observation of the lines of Fe II– III and Co II- III and tracking of the evolution of their relative strength in time (Kuchner et al. 1994; Dessart et al. 2014). In contrast, the mass of ^{56}Ni is only a few percent of the ejecta mass in SNe Ibc, so that at nebular times a significant part of the Fe II emission is from primordial Fe (a ^{56}Ni mass analogous to that inferred in SNe Ia is unlikely since in that case the nebular spectra would exhibit strong emission lines from iron-group elements). There also seems to be no strong Co line in the optical to infer an Fe/Co abundance ratio. This requires further investigation.

Models at the low-mass end, whose composition is dominated by He (i.e., models lighter than he3p5, although He content is not the only characteristics influencing the observables), seem to be in conflict with the currently observed properties of Type Ib SNe. These models exhibit strong N II lines and weak [O I] $\lambda\lambda$ 6300, 6364, while Type Ib and Type Ic SNe tend to show similar nebular phase spectra, with a tendency for weaker [O I] $\lambda\lambda$ 6300, 6364 in some Type Ib SNe (Fang et al. 2022). Although unlikely, this discrepancy could be an observational bias resulting from the lower ^{56}Ni mass in lower mass He-star explosions making such events harder to detect, and even

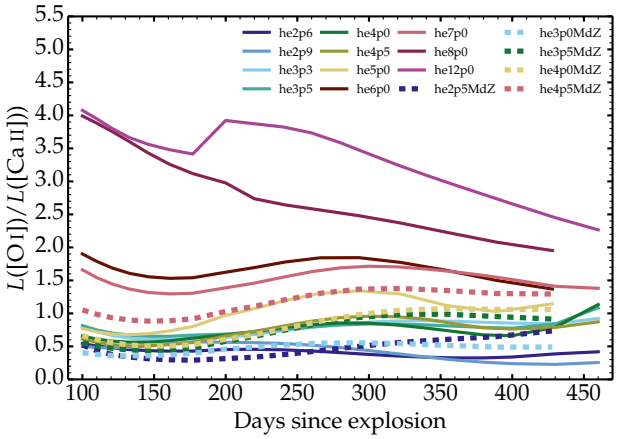

Fig. 8. Same as Fig. 5, but showing the ratio of the [O I] $\lambda\lambda$ 6300, 6364 flux with the [Ca II] $\lambda\lambda$ 7291, 7323 flux.

when found, less likely to be observed at nebular times. Another explanation may be that lower mass He-star models become He giants at the end of their lives (Yoon et al. 2012; Eldridge et al. 2015; McClelland & Eldridge 2016; Woosley 2019), enhancing the likelihood for mass transfer to a companion or for a common envelope phase (Laplace et al. 2020) – our He-star models were evolved in isolation from the He zero age main sequence until core collapse. In this case, such models could lead to ultra-stripped Type Ic SNe (Dewi & Pols 2003; Tauris et al. 2013) or to Type Ibn SNe (Pastorello et al. 2008; Hosseinzadeh et al. 2017; Dessart et al. 2022a). This possibility requires further study.

Our grid of 1D models exhibits a clear correlation between pre-SN mass and the ratio of the [O I] $\lambda\lambda$ 6300, 6364 flux with the [Ca II] $\lambda\lambda$ 7291, 7323 flux (Fig. 8). Such a correlation seems absent in observations (Fang et al. 2022; Prentice et al. 2022), although stripped-envelope SNe with weaker [O I] $\lambda\lambda$ 6300, 6364 tend to be of Type Ib (Fang et al. 2022). There may be various reasons for that. While the [O I] $\lambda\lambda$ 6300, 6364 flux arises from the O-rich shell, which is made prior to explosion, the [Ca II] $\lambda\lambda$ 7291, 7323 flux arises from the Fe/He and Si/S shells, which are both created or reset during explosive nucleosynthesis. The flux in both lines depends on the ^{56}Ni mass, and the flux in the [O I] $\lambda\lambda$ 6300, 6364 depends also on the ionization and clumping in the O-rich shell (Jerkstrand et al. 2015; D21). The distinct [O I]/[Ca II] flux ratio between models is probably driven from the large range in O-shell masses in our model set, which supersedes other dependencies.

The ejecta with the weakest [O I] $\lambda\lambda$ 6300, 6364 line flux arise from the lower mass He-star models, which are cooled primarily through Fe II and N II line emission, and for which (as noted earlier in this paper) there are currently no observational counterparts. Higher-mass He-star models in our grid are not favored by the initial mass function and may thus be rare in the observed sample of SNe Ibc. Hence, the lack of correlation in the observed [O I]/[Ca II] flux ratio might indicate that the bulk of SNe Ibc are of comparable and moderate pre-SN mass (or at least that the current sample of SNe Ibc pre-SN masses covers a reduced range relative to our model set). It also suggests that what distinguishes the majority of SNe Ib and Ic may not be so much the composition (i.e., total yields) but the large-scale mixing of ^{56}Ni and other elements such as He and O (Dessart et al. 2012). Further work is needed to quantify the role of large-scale mixing for the typing of stripped-envelope SNe.

Acknowledgements. This work was supported by the "Programme National de Physique Stellaire" of CNRS/INSU co-funded by CEA and CNES. D.J.H. thanks NASA for partial support through the astrophysical theory grant 80NSSC20K0524. H.K. was funded by the Academy of Finland projects 324504 and 328898. This work was granted access to the HPC resources of CINES under the allocation 2020 – A0090410554 and of TGCC under the allocation 2021 – A0110410554 made by GENCI, France. This research has made use of NASA's Astrophysics Data System Bibliographic Services.

References

Dessart, L. 2019, A&A, 621, A141
Dessart, L., & Audit, E. 2019, A&A, 629, A17
Dessart, L., & Hillier, D. J. 2020, A&A, 643, L13
Dessart, L., Hillier, D. J., Li, C., & Woosley, S. 2012, MNRAS, 424, 2139
Dessart, L., Hillier, D. J., Blondin, S., & Khokhlov, A. 2014, MNRAS, 439, 3114
Dessart, L., John Hillier, D., Yoon, S.-C., Waldman, R., & Livne, E. 2017, A&A, 603, A51
Dessart, L., Hillier, D. J., & Wilk, K. D. 2018, A&A, 619, A30
Dessart, L., Yoon, S.-C., Aguilera-Dena, D. R., & Langer, N. 2020, A&A, 642, A106
Dessart, L., Hillier, D. J., Sukhbold, T., Woosley, S. E., & Janka, H. T. 2021a, A&A, 656, A61
Dessart, L., John Hillier, D., Sukhbold, T., Woosley, S. E., & Janka, H. T. 2021b, A&A, 652, A64
Dessart, L., John Hillier, D., & Kuncarayakti, H. 2022a, A&A, 658, A130
Dessart, L., Prieto, J. L., Hillier, D. J., Kuncarayakti, H., & Hueichapan, E. D. 2022b, A&A, 666, L14
Dessart, L., Gutierrez, C. P., Kuncarayakti, H., Fox, O. D., & Filippenko, A. V. 2023, A&A, 675, A33
Dewi, J. D. M., & Pols, O. R. 2003, MNRAS, 344, 629
Drout, M. R., Soderberg, A. M., Gal-Yam, A., et al. 2011, ApJ, 741, 97
Eldridge, J. J., Fraser, M., Maund, J. R., & Smartt, S. J. 2015, MNRAS, 446, 2689
Ensman, L. M., & Woosley, S. E. 1988, ApJ, 333, 754
Ergon, M., & Fransson, C. 2022, A&A, 666, A104
Ertl, T., Woosley, S. E., Sukhbold, T., & Janka, H. T. 2020, ApJ, 890, 51
Fang, Q., Maeda, K., Kuncarayakti, H., et al. 2022, ApJ, 928, 151
Gabler, M., Wongwathanarat, A., & Janka, H.-T. 2021, MNRAS, 502, 3264
Hillier, D. J., & Dessart, L. 2012, MNRAS, 424, 252
Hosseinzadeh, G., Arcavi, I., Valenti, S., et al. 2017, ApJ, 836, 158
Jacobson-Galán, W. V., Dessart, L., Jones, D. O., et al. 2022, ApJ, 924, 15
Jerkstrand, A., Fransson, C., Maguire, K., et al. 2012, A&A, 546, A28
Jerkstrand, A., Ergon, M., Smartt, S. J., et al. 2015, A&A, 573, A12
Jerkstrand, A., Smartt, S. J., Inserra, C., et al. 2017, ApJ, 835, 13
Kleiser, I., Fuller, J., & Kasen, D. 2018, MNRAS, 481, L141
Kuchner, M. J., Kirshner, R. P., Pinto, P. A., & Leibundgut, B. 1994, ApJ, 426, L89
Laplace, E., Götberg, Y., de Mink, S. E., Justham, S., & Farmer, R. 2020, A&A, 637, A6
Laplace, E., Justham, S., Renzo, M., et al. 2021, A&A, 656, A58
Maguire, K., Jerkstrand, A., Smartt, S. J., et al. 2012, MNRAS, 420, 3451
Matheson, T., Filippenko, A. V., Barth, A. J., et al. 2000, AJ, 120, 1487
Maurer, I., Mazzali, P. A., Taubenberger, S., & Hachinger, S. 2010, MNRAS, 409, 1441
Mazzali, P. A., Nomoto, K., Patat, F., & Maeda, K. 2001, ApJ, 559, 1047
Mazzali, P. A., Maurer, I., Valenti, S., Kotak, R., & Hunter, D. 2010, MNRAS, 408, 87
McClelland, L. A. S., & Eldridge, J. J. 2016, MNRAS, 459, 1505
Pastorello, A., Mattila, S., Zampieri, L., et al. 2008, MNRAS, 389, 113
Podsiadlowski, P., Joss, P. C., & Hsu, J. J. L. 1992, ApJ, 391, 246
Prentice, S. J., Maguire, K., Siebenaler, L., & Jerkstrand, A. 2022, MNRAS, 514, 5686
Rho, J., Evans, A., Geballe, T. R., et al. 2021, ApJ, 908, 232
Silverman, J. M., Pickett, S., Wheeler, J. C., et al. 2017, MNRAS, 467, 369
Tauris, T. M., Langer, N., Moriya, T. J., et al. 2013, ApJ, 778, L23
Wheeler, J. C., & Levreault, R. 1985, ApJ, 294, L17
Wongwathanarat, A., Mueller, E., & Janka, H.-T. 2015, A&A, 577, A48
Woosley, S. E. 2019, ApJ, 878, 49
Woosley, S. E., Heger, A., & Weaver, T. A. 2002, Rev. Mod. Phys., 74, 1015
Woosley, S. E., Sukhbold, T., & Kasen, D. N. 2021, ApJ, 913, 145
Yoon, S.-C. 2015, PASA, 32, 15
Yoon, S.-C. 2017, MNRAS, 470, 3970
Yoon, S.-C., Gräfener, G., Vink, J. S., Kozyreva, A., & Izzard, R. G. 2012, A&A, 544, A11

Appendix A: Additional information

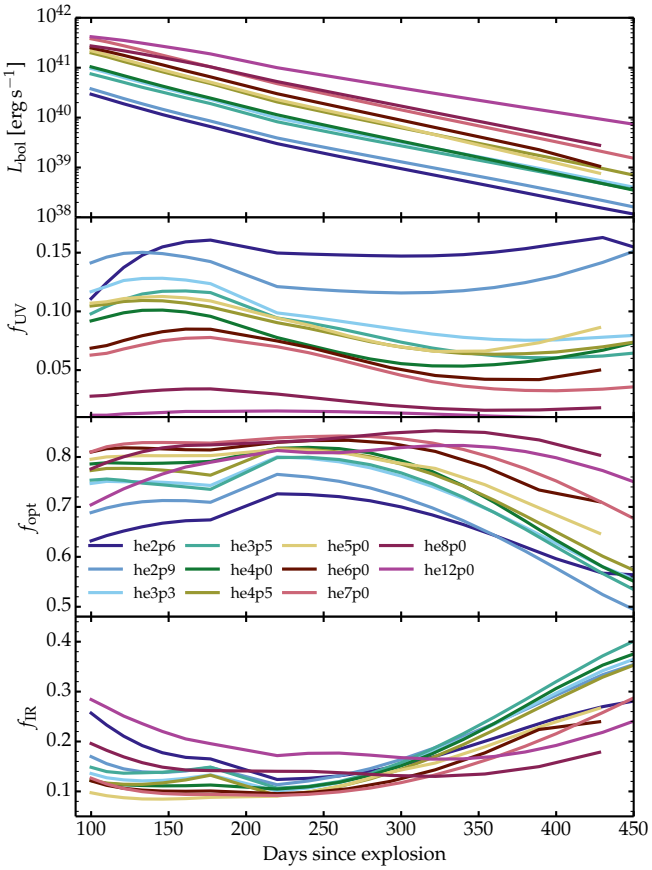

Fig. A.1. Evolution of the bolometric luminosity and the fraction of that luminosity falling in the UV, the optical, and the IR ranges as a function of time for the He-star explosion models from progenitors evolved with a nominal mass loss (see Woosley 2019; Ertl et al. 2020; D21).

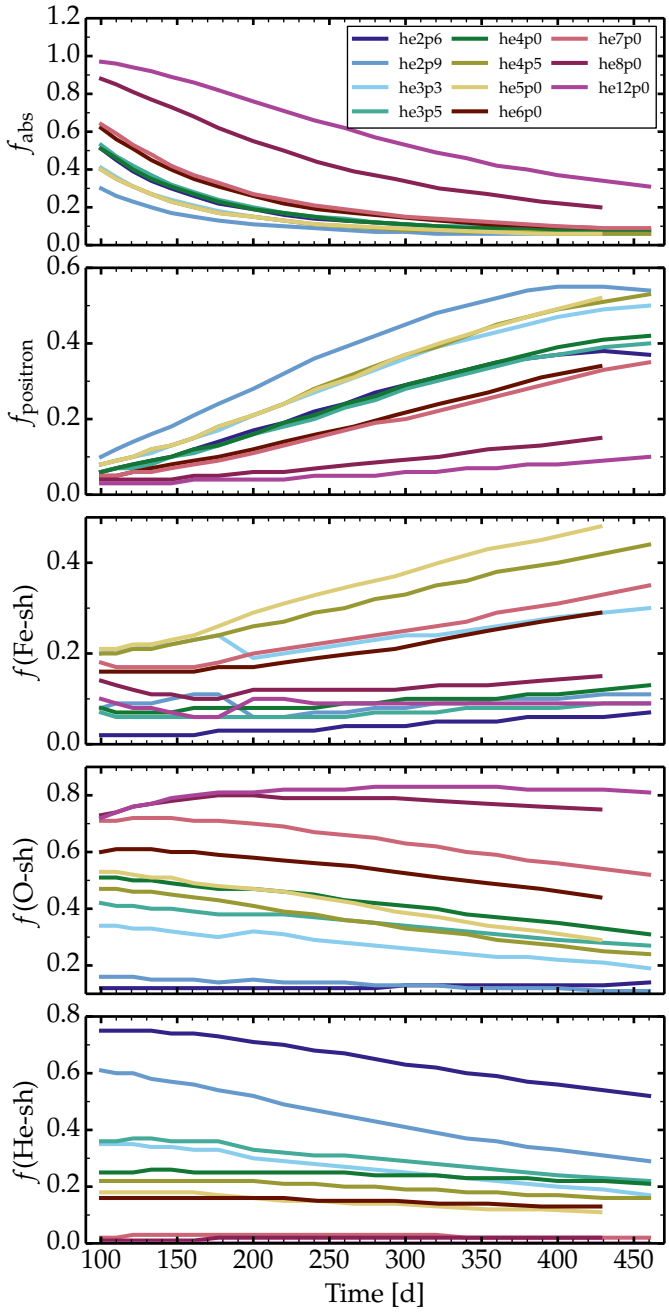

Fig. A.2. Evolution of the decay power absorbed in the ejecta, the fraction of that power that arises from positrons (assumed here to be absorbed locally), and the fraction of the total decay power absorbed by the Fe-rich, O-rich, and He-rich shells in models he2p6 to he12p0.

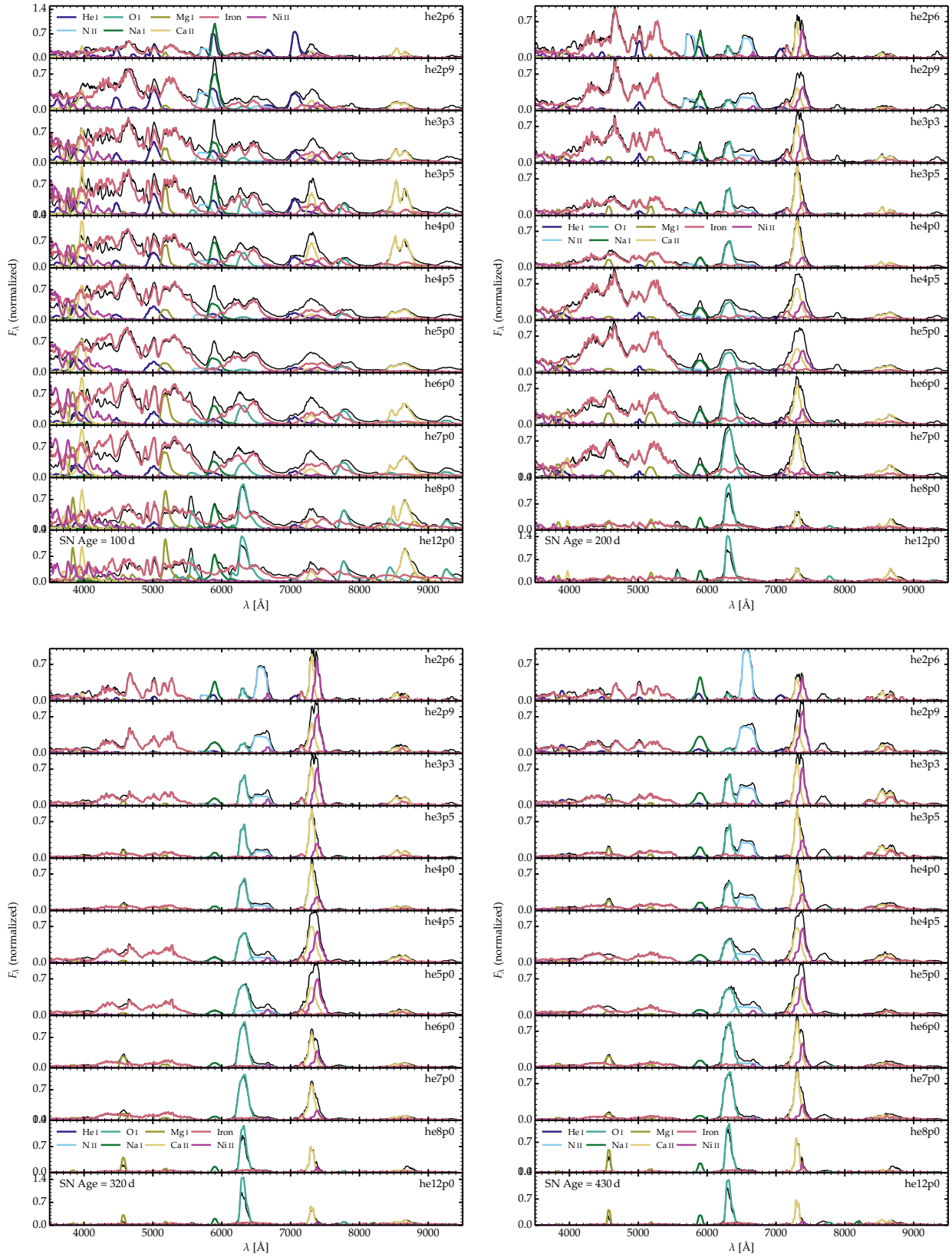

Fig. A.3. Comparison of optical spectra for He-star explosion models he2p6 to he12p0 at a SN age of 100 days (top left), 200 days (top-right), 320 days (bottom-left), and 430 days (bottom-right).

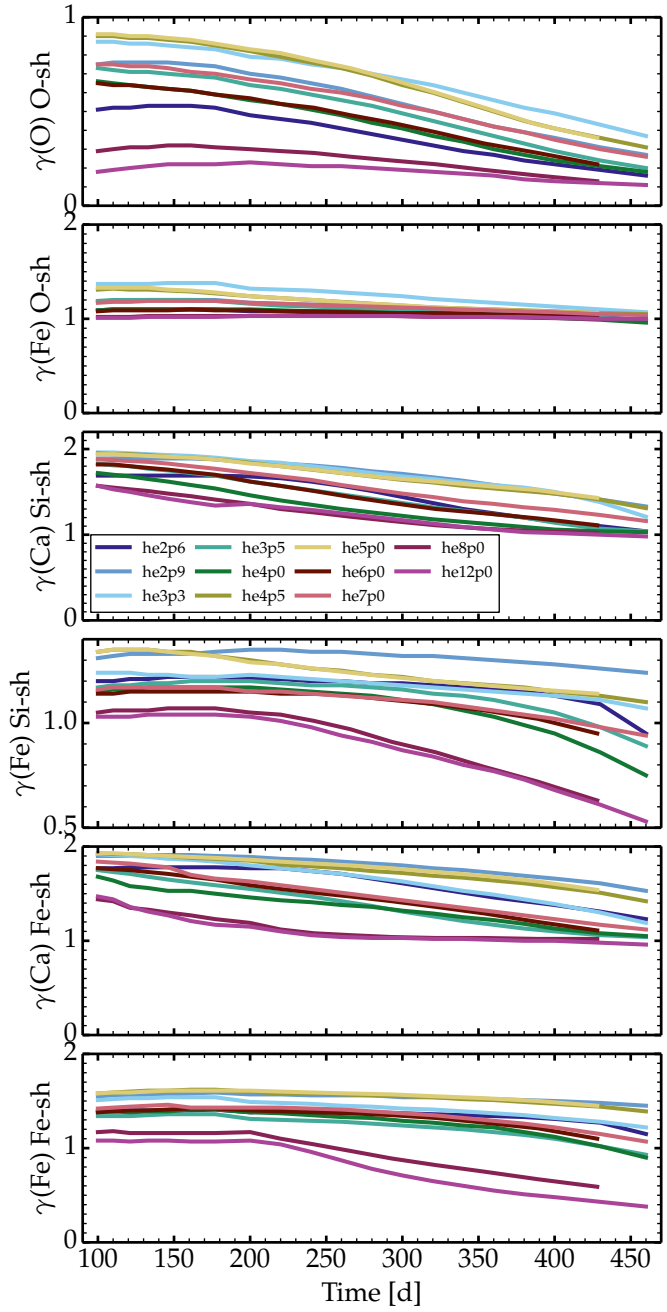

Fig. A.4. Evolution of the ionization of important species in the O-rich, Si-rich, and Fe-rich shells in models he2p6 to he12p0. The ionization in the He-rich shell (not shown here) is roughly constant in time and such that He is mostly neutral, N is mostly N^+, and Fe is mostly Fe^{2+}.

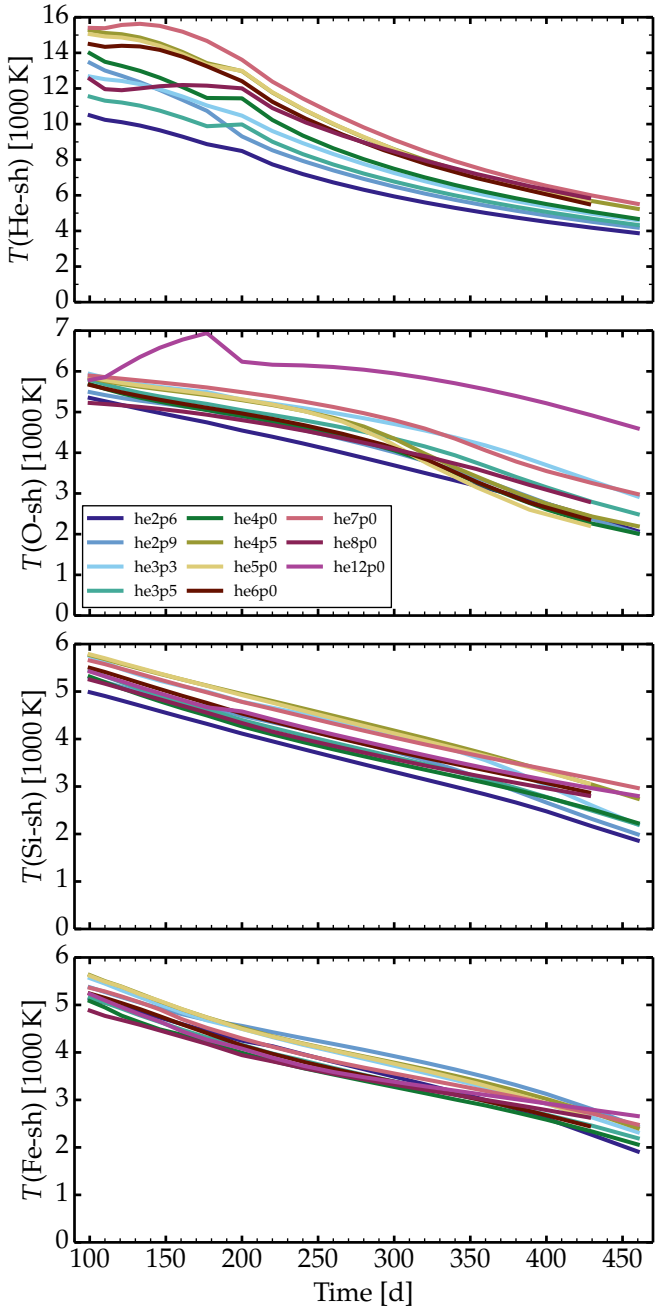

Fig. A.5. Evolution of the temperature of important species in the He-rich, O-rich, Si-rich, and Fe-rich shells in models he2p6 to he12p0 (the he12p0 model does not have a He-rich shell and thus no temperature is output for that model in the top panel).